

1 **Enisamium is an inhibitor of the SARS-CoV-2 RNA polymerase and shows**
2 **improvement of recovery in COVID-19 patients in an interim analysis of a**
3 **clinical trial**

4
5 Olha Holubovska^{1,11}, Denisa Bojkova^{2,11}, Stefano Elli^{3,11}, Marco Bechtel², David
6 Boltz⁴, Miguel Muzzio⁴, Xinjian Peng⁴, Frederico Sala³, Cesare Cosentino³, Alla
7 Mironenko⁵, Jens Milde⁶, Yuriy Lebed⁷, Holger Stammer⁶, Andrew Goy⁸, Marco
8 Guerrini³, Lutz Mueller^{9*}, Jindrich Cinatl^{2*}, Victor Margitich^{8*}, and Aartjan J. W. te
9 Velthuis^{10,11*}

10
11 ¹O.O. Bogomolets National Medical University, T. Shevchenko blvd., 13, Kyiv,
12 Ukraine

13 ²Institute of Medical Virology, University Hospital Frankfurt, Goethe University,
14 Frankfurt am Main, Germany

15 ³Istituto di Ricerche Chimiche e Biochimiche "G. Ronzoni", Via Giuseppe Colombo
16 81, 20133 Milano, Italy

17 ⁴IIT Research institute, 10 W 35th St, Chicago, IL 60616, United States

18 ⁵L.V. Gromashevsky Institute of Epidemiology and Infectious Diseases of the NAMS
19 of Ukraine, Department of respiratory and other viral infections, Amosova str 5a,
20 03083, Kyiv, Ukraine

21 ⁶Pharmalog Institut für klinische Forschung GmbH, Ismaning, Germany

22 ⁷Pharmaxi LLC, Filatova Str., 10A, office 3/20, 01042, Kyiv, Ukraine

23 ⁸Farmak Joint Stock Company, Kyrylivska Street, 04080, Kyiv, Ukraine

24 ⁹Dr. Regenold GmbH, Zöllinplatz 4, D-79410 Badenweiler, Germany

25 ¹⁰Division of Virology, Department of Pathology, Addenbrooke's Hospital, University
26 of Cambridge, Hills Road, CB2 2QQ, United Kingdom

27 ¹¹These authors contributed equally

28
29 *Corresponding authors. E-mail: ajwt6@cam.ac.uk, cinatl@em.uni-frankfurt.de,
30 lutz.mueller@regenold.com, v.margitich@farmak.ua

31
32 **Key words:** Covid-19, SARS-CoV-2, molecular dynamics simulation, RNA
33 polymerase, FAV00A, Amizon

34
35
36 Phase III clinical trial registered at ClinicalTrials.gov under number NCT04682873.

37

38 **Abstract**

39 Pandemic SARS-CoV-2 causes a mild to severe respiratory disease called
40 Coronavirus Disease 2019 (COVID-19). Control of SARS-CoV-2 spread will depend
41 on vaccine-induced or naturally acquired protective herd immunity. Until then,
42 antiviral strategies are needed to manage COVID-19, but approved antiviral
43 treatments, such as remdesivir, can only be delivered intravenously. Enisamium
44 (laboratory code FAV00A, trade name Amizon®) is an orally active inhibitor of
45 influenza A and B viruses in cell culture and clinically approved in countries of the
46 Commonwealth of Independent States. Here we show that enisamium can inhibit
47 SARS-CoV-2 infections in NHBE and Caco-2 cells. *In vitro*, the previously identified
48 enisamium metabolite VR17-04 directly inhibits the activity of the SARS-CoV-2 RNA
49 polymerase. Docking and molecular dynamics simulations suggest that VR17-04
50 prevents GTP and UTP incorporation. To confirm enisamium's antiviral properties,
51 we conducted a double-blind, randomized, placebo-controlled trial in adult,
52 hospitalized COVID-19 patients, which needed medical care either with or without
53 supplementary oxygen. Patients received either enisamium (500 mg per dose) or
54 placebo for 7 days. A pre-planned interim analysis showed in the subgroup of
55 patients needing supplementary oxygen (n = 77) in the enisamium group a mean
56 recovery time of 11.1 days, compared to 13.9 days for the placebo group (log-rank
57 test; p=0.0259). No significant difference was found for all patients (n = 373) or those
58 only needing medical care (n = 296). These results thus suggest that enisamium is
59 an inhibitor of SARS-CoV-2 RNA synthesis and that enisamium treatment shortens
60 the time to recovery for COVID-19 patients needing oxygen.

61

62 **Significance statement**

63 SARS-CoV-2 is the causative agent of COVID-19. Although vaccines are now
64 becoming available to prevent SARS-CoV-2 spread, the development of antivirals
65 remains necessary for treating current COVID-19 patients and combating future
66 coronavirus outbreaks. Here, we report that enisamium, which can be administered
67 orally, can prevent SARS-CoV-2 replication and that its metabolite VR17-04 can
68 inhibit the SARS-CoV-2 RNA polymerase *in vitro*. Moreover, we find that COVID-19
69 patients requiring supplementary oxygen, recover more quickly than patients treated
70 with a placebo. Enisamium may therefore be an accessible treatment for COVID-19
71 patients.

73 **Introduction**

74 Severe acute respiratory coronavirus 2 (SARS-CoV-2) is an important human
75 pathogen and the causative agent of COVID-19. Vaccines are available to prevent
76 the spread of SARS-CoV-2, and several antiviral strategies, such as treatment with
77 remdesivir or convalescent plasma, have received emergency approval. However,
78 the development of additional strategies remains necessary since vaccine roll-out is
79 slow and current treatments can only be delivered intravenously. A key target for
80 novel drug screening is the RNA polymerase of SARS-CoV-2 (1-4).

81 SARS-CoV-2 is a betacoronavirus and contains a positive-sense, non-
82 segmented RNA genome of around 30 kilobases (5, 6). The 5' two-thirds of the viral
83 genome encode two overlapping open reading frames (ORFs), 1a and 1b, which are
84 translated into two large polyproteins by host cell ribosomes. The two polyproteins
85 are cleaved by intrinsic proteolytic activity to produce 16 non-structural proteins
86 (nsps). Nsp12 is the RNA-dependent RNA polymerase that copies and transcribes
87 the SARS-CoV-2 genome (7, 8). Nsp12 requires nsp7 and nsp8 for processivity *in*
88 *vitro* (9) and likely other nsps, such as nsp9 and nsp13, for processivity *in vivo*. The
89 structures of nsp12/7/8 and nsp8/9/12/13 complexes from SARS-CoV and SARS-
90 CoV-2 have been solved by cryo-EM (10-12).

91 Remdesivir has been shown to inhibit the SARS-CoV-2 nsp12/7/8 complex
92 and other nucleoside analogue drugs or small molecule inhibitors have been
93 suggested as therapeutic candidates (1-3). One of the drugs highlighted by the
94 World Health Organisation as a candidate therapeutic against SARS-CoV-2 is
95 enisamium (4-(benzylcarbamoil)-1-methylpyridinium) iodide (laboratory code
96 FAV00A, marketed as Amizon®; Fig. 1A). Enisamium is licensed for use in 11
97 countries and a recent study found that enisamium is hydroxylated in humans and
98 human lung cells to a compound called VR17-04 (Fig. 1A). VR17-04 inhibits the
99 activity of the influenza virus RNA polymerase and reduces viral shedding and
100 improves patient recovery in influenza patients (13).

101 In this study, we show that enisamium metabolite VR17-04 inhibits the SARS-
102 CoV-2 nsp12/7/8 complex *in vitro*, likely by preventing incorporation of GTP and
103 UTP. We also show that parent compound enisamium inhibits SARS-CoV-2 growth
104 on Caco-2 and NHBE cells. In patients needing medical care and supplementary
105 oxygen COVID-19 (Severity Rating 4 [SR 4] of the modified WHO ordinal scale),
106 enisamium significantly improved the time to recovery compared to a placebo

107 control. These data imply that enisamium is a possible therapeutic option for treating
108 SARS-CoV-2 infection.

109

110 **Results**

111 *Enisamium inhibits SARS-CoV-2 infection in cell culture*

112 Previous experiments showed that enisamium (Fig. 1A) can efficiently inhibit
113 influenza virus replication in normal human bronchial epithelial (NHBE) cultures and
114 A549 cells, and to a lesser extent in Caco-2 cells (13). Previous experiments have
115 also demonstrated that enisamium is not cytotoxic to these cells (13). To test if
116 enisamium can inhibit pandemic SARS-CoV-2 replication in cell culture, we first
117 incubated Caco-2 cells, a standard cell-line for SARS-CoV-2 infection *in vitro*, with
118 enisamium iodide or enisamium chloride for 6 hours and subsequently infected the
119 treated cells with SARS-CoV-2. After 48 hours, inhibition of viral infection was
120 assessed by antigen staining for viral nucleoprotein expression and RT-qPCR for
121 viral genome replication. We observed a significant reduction in both viral
122 nucleoprotein expression (Fig. 1B), a reduction in the cytopathic effect of the SARS-
123 CoV-2 infection on Caco-2 cells (Fig. 1C), and a 2-log reduction in the number of
124 viral genome copies in the infected cells as a function of the enisamium
125 concentration (Fig. S1). The IC_{50} for enisamium chloride in Caco-2 cells was 1.2 mM
126 (~300 $\mu\text{g/ml}$), which is comparable to the inhibitory effect of enisamium on influenza
127 A virus replication in Caco-2 cells (13). To test if enisamium inhibited SARS-CoV-2
128 replication in NHBE cells, NHBE cells were incubated with enisamium iodide for 6
129 hours and subsequently infected with SARS-CoV-2. Analysis of the viral RNA levels
130 in infected NHBE cells revealed an IC_{50} of 250 $\mu\text{g/ml}$ (Fig. 1D). We obtained
131 comparable results in NHBE cells infected with alpha-coronavirus HCoV NL63 (Fig.
132 1E), implying that enisamium can inhibit coronavirus replication.

133

134 *Enisamium and VR17-04 inhibit SARS-CoV-2 nsp12/7/8 activity*

135 Previous experiments showed that enisamium and VR17-04 can inhibit the influenza
136 A virus RNA polymerase *in vitro* (13). To determine if enisamium and its putative
137 metabolite VR17-04 can inhibit the SARS-CoV-2 RNA polymerase, we used a
138 SARS-CoV-2 RNA polymerase *in vitro* assay that involved nsp12 as the RNA-
139 dependent RNA polymerase, and nsp7 and nsp8 as processivity factors. We
140 expressed and purified SARS-CoV-2 nsp7, nsp8 and nsp12, and mixed them at a

141 ratio of 2:2:1 to form a nsp12/7/8 complex. Next, we incubated the nsp12/7/8
142 complex with a hairpin template (Fig. 1F) in the presence of 0.5 mM of each
143 nucleotide triphosphate (NTP) and varying concentrations of enisamium or the
144 previously identified enisamium metabolite VR17-04. Enisamium inhibited nsp12/7/8
145 activity at relatively high concentrations, with an IC₅₀ of 26.3 mM (Fig. 1G). By
146 contrast, VR17-04 had an estimated IC₅₀ of 0.98 mM on the hairpin template (Fig.
147 1G). These IC₅₀ values are within an order of magnitude of those observed for the
148 inhibition of the influenza virus RNA polymerase (13). Moreover, the IC₅₀ value for
149 VR17-04 on SARS-CoV-2 nsp12/7/8 is similar to remdesivir triphosphate in the
150 presence of 0.5 mM NTPs in a comparable assay (14). A 10-fold reduction of the
151 NTP concentration in the assay lowered the VR17-04 IC₅₀ value to 0.029 mM (Fig.
152 1G), suggesting that VR17-04 is competing with NTP incorporation. Collectively,
153 these data suggest that RNA synthesis by the SARS-CoV-2 nsp12/7/8 complex is
154 inhibited by enisamium and its metabolite VR17-04 *in vitro*.

155

156 *Enisamium forms hydrogen bonds with adenine and cytosine in nsp12 and influenza* 157 *polymerase active site*

158 Previous studies (13, 15) and our data in Fig. 1A, suggest that enisamium acts
159 through metabolite VR17-04 and inhibits the activity of the influenza A virus and
160 SARS-CoV-2 nsp12 RNA polymerases. However, the mechanism of RNA synthesis
161 inhibition by VR17-04 is not fully understood. We hypothesised that the additional
162 OH-group of VR17-04 could support hydrogen bond formation with adenine and
163 cytosine (Fig. 2A), creating two hydrogen bonds in total, while enisamium would form
164 only one hydrogen bond with these bases. We expected that VR17-04 would not
165 form hydrogen bonds with guanine or uridine (Fig. S2), suggesting that the inhibitory
166 effect of VR17-04 would be dependent on the template sequence.

167 The CO and OH groups of VR17-04 can adopt *trans* and *eclipsed*
168 conformations that are characterized by three dihedral angles: ϕ_1 , ϕ_2 and ϕ_3 (Fig. 2B).
169 Dihedral angles ϕ_1 and ϕ_2 are also present in enisamium, but ϕ_3 involves different
170 atoms (Fig. S4). In VR17-04, dihedral angle ϕ_3 is $\sim 180^\circ$ in the *trans* conformation
171 and $\sim 0^\circ$ in the *eclipsed* conformation (Fig. 2B). Based on quantum chemical
172 calculations, the *eclipsed* conformation has a lower energy than the *trans*
173 transformation (Table S1), and only the *eclipsed* conformation would be compatible

174 with cytosine or adenosine binding (Fig. 2B). To confirm that VR17-04 can adopt the
175 *eclipsed* conformation in solution, we measured the ^1H NOESY spectrum of VR17-
176 04 in water and found a correlation between the protons 'HN' and 'H5' that is
177 compatible with a ϕ_3 value of 0° (Fig. 2C). The chemical shifts of the selected
178 protons are reported in Table S2. Additionally, we observed a correlation between
179 the HN and the CH_2 , or the ortho aromatic protons of the Ph group (Fig. 2C). These
180 observations suggest that VR17-04 can adopt a conformation that would be
181 compatible with hydrogen bond formation with cytosine and adenine.

182 To further investigate whether VR17-04 can inhibit the activity of the SARS-
183 CoV nsp12 RNA polymerases through base-pair interactions with the template, we
184 docked enisamium or VR17-04 into the SARS-CoV-2 nsp12/7/8 complex bound to
185 template RNA and remdesivir monophosphate (PDB 7bv2, Fig. 2D). Prior to
186 docking, we removed the remdesivir monophosphate from the complex, and used
187 *in silico* mutagenesis to change the uridine in the active site to cytosine or adenine.
188 After selection of the most significant poses, we found that both enisamium and
189 VR17-04 can be accommodated in the +1 position of the nucleotide binding pocket
190 (Fig. 2E-G), in a position similar to remdesivir monophosphate (Fig. 2D). VR17-04
191 was specifically coordinated through hydrogen bond interactions with the unpaired
192 cytosine residue of the template RNA. Nsp12 residues K545 and K555 were
193 predicted to preserve the VR17-04 position in the catalytic cavity (Fig. S4). In
194 addition, our modelling suggests that VR17-04 can form a stacking interaction with
195 the -1 base of the nascent strand. By contrast, enisamium docked in the same +1
196 nascent strand position, but only formed one hydrogen bond with the cytosine in the
197 +1 template position (Fig. S4).

198 To estimate the binding stability of enisamium or VR17-04 in the nsp12 active
199 site, we performed molecular dynamics (MD) simulations of enisamium or VR17-04
200 in the nsp12 active site (see Material and Methods for specifics). Our MD simulations
201 predict that VR17-04 favourably binds the unpaired cytosine in the +1 position of
202 nsp12/7/8 complex, maintaining two hydrogen bonds (Watson-Crick base pair) as
203 seen by the preserved hydrogen bonds distances (Fig. 2 E-G) and the coplanarity
204 angle (Fig. 2H, I). By contrast, our simulations predict that enisamium binds less
205 stably to the nsp12/7/8 complex, based on the ~2-fold difference in distance between
206 enisamium and cytosine compared to VR17-04 and cytosine (Fig. 2E, F; Table S3),

207 and a higher estimated Poisson-Boltzmann free energy for the enisamium binding
208 (43.6 kcal/mol) compared to VR17-04 binding to either cytosine (-19.8 kcal/mol) or
209 adenine (-14.8 kcal/mol) (Table S4).

210 To investigate if VR17-04 inhibits the SARS-CoV nsp12/7/8 RNA polymerase
211 complex in a sequence-specific manner, we analysed the extension of a hairpin
212 template containing a cytosine or adenine in the +1 position of the template (Fig. 2J)
213 in the presence or absence of VR17-04. We found that at high VR17-04
214 concentrations, the nsp12/7/8 RNA polymerase complex was prevented from
215 incorporating GTP and UTP (Fig. 2J). When we subsequently moved the cytosine
216 residue to the +2 nt position of the template down and introduced a uridine at the +1
217 position, ATP was incorporated in the presence of VR17-04 but GTP was not (Fig.
218 2K), suggesting that the inhibitory activity of VR17-04 is dependent on the sequence
219 of the template.

220

221 *Enisamium Improves COVID-19 Patient Recovery in Interim Analysis of Clinical Trial*

222 To investigate if enisamium affects the clinical course of COVID-19 patients, a
223 double-blind, randomized, placebo-controlled phase III clinical study was performed.
224 The COVID-19 diagnosis was based on a body temperature of ≥ 37.8 °C and
225 laboratory confirmed presence of SARS-CoV-2 RNA by RT-PCR in pharyngeal
226 swabs or sputum. The patient cohorts required either medical care but no
227 supplementary oxygen (Severity Rating (SR) 5; WHO score 3), or medical care and
228 supplementary oxygen (SR 4; WHO score 4) on the day of enrolment and
229 randomization. Randomized COVID-19 patients were treated with either placebo
230 (group A) or enisamium chloride (group B) for 7 days. The chosen primary endpoint
231 of the trial was time-to-recovery, and recovery was defined as an improvement in the
232 SR baseline status by 2 SR score values (e.g., a change from SR 4 to SR 6).

233 In accordance with the study protocol, an interim analysis on all patients in the
234 Intent-to-Treat evaluation set (ITT) was performed for the primary endpoint by an
235 Independent Data Monitoring Committee (IDMC) using a pre-defined Charter. The
236 ITT set for interim analysis included 373 patients of which 296 patients had SR 5 and
237 77 patients had SR 4 on day of randomization (Fig. 3A). The interim analysis showed
238 no difference in time-to-recovery and median time-to-recovery between all placebo-
239 and enisamium-treated ITT patients (Fig. 3B) nor in the subgroup of patients with SR
240 5 (Fig 3C). In contrast, analysis of the SR 4 subgroup alone (n = 77) revealed a

241 faster time-to-recovery with the enisamium-treated patients compared to the
242 placebo-treated for the whole period of recovery, starting 7 days after randomization
243 (Fig. 3D). The estimated median time-to-recovery was 13 days for the placebo-
244 treated patients and 11 days for the enisamium-treated patients. The mean time-to-
245 recovery was 13.9 days for the placebo-treated group and 11.1 days for the
246 enisamium-treated group. The log-rank test showed a significant advantage in
247 recovery time in favour of enisamium treatment at interim stage ($P = 0.0259$). The
248 maximum time-to-recovery was reached on day 21 for the enisamium-treated group.
249 Not all patients recovered in the placebo-treated group. For these patients, the
250 recovery time was displayed as 29 days (Fig. 3D).

251 Based on the above findings, the IDMC recommended to stop recruitment of
252 patients requiring only medical care but no oxygen (SR 5; WHO score 3) and to
253 continue the study with COVID-19 patients requiring supplementary oxygen in
254 addition to standard medical care (SR 4; WHO score 4).

255

256

257 Discussion

258 The rapid global spread of SARS-CoV-2 necessitates development of effective
259 therapeutic interventions, and the most promising short-term strategy is to repurpose
260 existing drugs. In this study we showed that enisamium, which is approved for use
261 against influenza in 11 countries, can inhibit SARS-CoV-2 RNA synthesis (Fig. 1).
262 Moreover, we showed that enisamium and its metabolite, VR17-04, inhibit the RNA
263 synthesis activity of the SARS-CoV-2 nsp12/7/8 complex (Fig. 1, 2). Molecular
264 dynamics analysis and *in vitro* activity assays suggest that VR17-04 prevents GTP
265 and UTP incorporation into the nascent RNA chain (2).

266 It was previously reported that enisamium inhibits the influenza A virus RNA
267 polymerase activity *in vitro* with a relatively high IC_{50} value of 46.3 mM (13). This
268 inhibition was improved 55-fold by addition of a hydroxyl group in the compound
269 VR17-04 (13). We find that SARS-CoV-2 nsp12/7/8 complex activity is inhibited by
270 enisamium and VR17-04 with similar IC_{50} values to the influenza A virus RNA
271 polymerase at similar NTP levels (Fig. 1) (13). Furthermore, the IC_{50} value for VR17-
272 04 is similar to remdesivir triphosphate in a similar *in vitro* assay used (14).
273 Remdesivir triphosphate is the active metabolite of remdesivir, which has shown

274 promise in both cell culture and clinical trials as a treatment for SARS-CoV-2
275 infection (16).

276 Our docking and molecular dynamics simulations suggest that VR17-04 can
277 bind a template cytosine or adenine base in the active site of the SARS-CoV-2 RNA
278 polymerase. This hypothesis is supported by our NOE experiments performed in
279 water, which indicate that VR17-04 can adopt an *eclipsed* conformation in solution.
280 Only the *eclipsed* conformation is compatible with the sequence-specific inhibition
281 we observed in our *in vitro* polymerase reactions. We cannot fully exclude the
282 possibility that VR17-04 can also bind bases in the nascent RNA strand. However,
283 we think that this alternative explanation does not adequately explain our data.

284 We observed that the inhibitory effect of enisamium was more pronounced in
285 NHBE cells than in Caco-2 cells, which is in line with previous influenza A virus
286 experiments (13, 15) and suggest that enisamium is more readily metabolised into
287 VR17-04 in primary bronchial epithelial cells compared to adenocarcinoma cells.
288 Interestingly, the interim phase III clinical trial results that we disclose here reveal a
289 faster improved recovery in COVID-19 patients needing supplementary oxygen,
290 strongly suggesting that our *in vitro* data are well-aligned with the data from the
291 clinical trial. We cannot exclude that enisamium or its metabolite has effects beyond
292 RNA polymerase inhibition and that these additional effects contribute to the COVID-
293 19 patient recovery.

294 Overall, our results strongly suggest that enisamium metabolite VR17-04
295 inhibits RNA synthesis by the SARS-CoV-2 nsp12/7/8 complex. Together with the
296 interim phase III clinical trial findings that enisamium improved the recovery of
297 COVID-19 needing supplementary oxygen (SR 4) by more than 2 days, our
298 observations raise the possibility that enisamium could be used a viable therapeutic
299 option against SARS-CoV-2 infection. Moreover, unlike remdesivir, enisamium does
300 not require intravenous administration, which would be advantages for its use
301 outside of a hospital setting. Together with observations that enisamium can inhibit
302 other RNA virus infections, and DNA virus infections (13, 15, 17), these results here
303 suggest that it can act as broad-spectrum polymerase inhibitor.

304

305

306 **Materials and Methods**

307 ***SARS-CoV-2 infections***

308 Confluent layers of Caco-2 cells in 96-well plates were treated with serial dilutions of
309 FAV00A or FAV00B 6 hours prior to infection. The cells were infected with SARS-
310 CoV-2 at multiplicity of infection 0.01 for 1 h, and compound reapplied following virus
311 removal. At 48h post infection, the cytopathic effect was recorded by examination of
312 infected cultures by light microscopy and supernatant collected to quantify virus RNA
313 by RT-qPCR as described previously, using nsp12-specific primers 5'-
314 GTGARATGGTCATGTGTGGCGG-3' and 5'-
315 CARATGTTAAASACACTATTAGCATA-3' (18-20). Cells were fixed with
316 acetone/methanol (40:60) and immunostained using a SARS-CoV-2 nucleoprotein
317 monoclonal antibody (1:500, Sinobiological, Cat #40143-R019-100ul). Staining was
318 detected using a peroxidase conjugated anti-rabbit secondary antibody (1:1000,
319 Dianova) and the addition of AEC substrate.

320

321 ***HCoV-NL63 NHBE infections***

322 MatTek's EpiAirway System (MatTek; Ashland, MA) consisted of differentiated
323 NHBE cells that were cultured to form a multilayered, highly differentiated model that
324 closely resembles the epithelial tissue of the respiratory tract. The cells from a single
325 donor (No. 9831) were used for assay consistency. The apical surface of the cells
326 was exposed to a humidified 95% air/ 5% CO₂ environment. The basolateral
327 medium was changed, and the mucin layer was washed every 24-48 hours. NHBE
328 cells were inoculated via the exposure of the apical side to HCoV-NL63. After 1 hour
329 of incubation with virus in a water-jacketed 37°C incubator with a 5% CO₂ supply,
330 the viral inoculum was removed from the cells. The apical side of the cells was
331 washed once prior to infection. After viral inoculation, enisamium chloride or control
332 media were added to the apical side of the cells and the basal media compartment
333 and incubated with the cells for 1 hour. After a 1-hour incubation, the drug containing
334 media was removed from apical and basal chambers. Growth medium alone or
335 growth medium with enisamium chloride were added to the bottom chamber, and
336 cells were incubated for 48 hours. At the termination of the experiments, cells were
337 washed twice, then 1 ml Trizol (Invitrogen) was added to each well for RNA isolation.
338 Total RNA was isolated from cells using Trizol per the manufacturer's instruction.
339 Two-step RT-qPCR was performed using HCoV-NL63 N gene-specific primers/probe
340 (forward primer: 5'-TGGTGTGTTGTTGGGTTGCTA-3', reverse primer 5'-
341 GCTCTGGAGGCAAAGCAATA-3', double-quenched probe: 5'-

342 FAM/CGCAAACGT/ZEN/AATCAGAAACCTTTGGA/IABKFQ-3'), GAPDH was analysed
343 at the same time with GAPDH-specific primers (5'- GTTCGACAGTCAGCCGCATC-
344 3' and 5'- AGTTAAAAGCAGCCCTGGTGA-3') by RT-qPCR and served as a
345 reference gene for normalization.

346

347 ***SARS-CoV-2 nsp12/7/8 in vitro activity assays***

348 Plasmids expressing nsp7, nsp8 and nsp12 were kindly provided by Dr Ervin Fodor
349 (University of Oxford). Nsp7, nsp8 and nsp12 were purified as described previously
350 (14) and mixed at a molar ratio of 2:2:1 to form active nsp12/7/8 complex. For activity
351 assays, 50 nM hairpin template (5'-
352 CGUAGGAGAAUGACAAAUUUUGUCAUUCUCC-3'), or a variation of this
353 template (see figures), was incubated with 1 μ M nsp12/7/8 complex for 30 mins at 30
354 $^{\circ}$ C, in reaction buffer containing 5 mM $MgCl_2$, 20 mM HEPES pH 8.0, 0.5 mM ATP,
355 0.5 mM UTP, 0.5 mM GTP, 0.5 mM CTP, 0.05% NP-40, 5% glycerol, 50 mM NaCl, 1
356 U RNasin (Promega) and 1 mM DTT. Hairpin templates were based on the 3'
357 terminal sequence of the SARS-CoV-2 genome and reference (3). Reactions were
358 stopped by addition of 80% formamide and 10 mM EDTA, followed by heating to 95
359 $^{\circ}$ C for 3 min. Reaction products were resolved by 20 % denaturing PAGE with 7M
360 urea, and visualised by phosphorimaging on a Typhoon FLA 7000 (GE Healthcare)
361 scanner. Data were analysed using ImageJ and Prism 9 (GraphPad). Enisamium
362 iodide (Farmak) or VR17-04 (Farmak) were dissolved in DMSO to a stock
363 concentration of 250 and 125 mg/ml, respectively. Dilutions were made in DMSO.

364

365 ***NOE NMR spectra measurement***

366 The VR17-04 (2 mg) was dissolved in 0.6 ml D₂O/water solution (5% D₂O). NMR
367 experiments were performed at 500MHz at 277 K. For NOESY experiments
368 (noesygpph) 128 transients were collected for each free-induction decay, using a
369 mixing time of 300 ms and 20 sec of relaxation delay. NOESY experiment (matrix
370 1024 · 320 points) was zero-filled to 2K · 2K before Fourier transformation.
371 Measurements were taken on a Bruker 500 HD NMR spectrometer equipped with a
372 5 mm BB probe.

373

374 ***Conformational characterization and geometry optimization***

375 The VR17-04 and enisamium conformational characterization and geometry
376 optimization was done using the quantum chemical approach DFT B3LYP/6-31G*.
377 The lowest energy conformation of VR17-04 (ϕ_3 eclipsed) and enisamium were
378 selected for further docking and for partial charge estimation (Table S1).

379

380 **Molecular docking**

381 The docking simulation was performed using Autodock 4.2 software (21). The
382 geometry of the ligands was previously optimized by DFT B3LYP/6-31G*. The
383 geometry of the receptor RdRp was extracted from the PDB 7bv2 (22). The catalytic
384 site of the nsp12/7/8 complex include the template RNA strand, the nascent strand
385 RNA, the pyrophosphate moiety $[\text{O}_3\text{P-O-PO}_3]^{-4}$ (pyr) and two Mg^{+2} ions, whose
386 positions were included in 7BV2. The two Zn^{+2} ions that were co-crystallized in 7BV2
387 were also included in the models. The co-crystallized inhibitor remdesivir was
388 removed from the complex, while its position and the contacts with the template RNA
389 through the unpaired uracil base in the +1 position were used to guide the molecular
390 docking. The unpaired uracil base was subsequently mutated in cytosine (Cyt) or
391 adenine (Ade) in Pymol 2.3.4 (Schrodinger LLC), generating two different
392 complexes, identified as nsp12/7/8(Cyt) and nsp12/7/8(Ade) respectively. Next,
393 Gasteiger charges were calculated for both ligands (VR17-04, enisamium) and the
394 receptor complexes, and used as parameters of the docking simulation (23). In the
395 docking simulation VR17-04 and enisamium were described by five and four
396 rotational degrees of freedom, respectively. The docking gridbox was built by
397 orthogonal hedges of length between 60 to 80 points. The gridbox centre was set to
398 the NH_2^- group of the target cytosine or adenine residues of the template RNA
399 strand, respectively, and further set-up to fit the space between the R555 and K545,
400 and the uracil of the nascent RNA strand. The docking runs used the default Genetic
401 Algorithm search, with parameters: number of GA runs, population size, max number
402 of energy evaluation, and max number of generations set as 100, 2000, $2.5 \cdot 10^7$,
403 270.000. At each run the docking solutions were clustered using a tolerance RMSD
404 = 2.0 Å. Three different docking simulations were run: VR17-04 and enisamium were
405 docked on to nsp12/7/8(Cyt), while, for comparison, VR17-04 was further docked on
406 nsp12/7/8(Ade). The docking solutions were selected based on two criteria. The first
407 criterium was the possibility to form a Watson-Crick base-pair interaction between

408 VR17-04 (or enisamium) and the unpaired cytosine or adenine. The second criterium
409 was based on the possibility to figure out interferences of the ligand with the catalytic
410 mechanism, for example by interaction with key residues of the nsp12/7/8 complex.
411 The selected poses were further ranked by preliminary MD simulation (approximately
412 20 ns) in explicit solvent, to predict the stability of the interaction, and to estimate the
413 Poisson-Boltzmann free energy of binding, this last property was used to obtain a
414 final selection and ranking of the poses.

415

416 ***Molecular dynamic simulation***

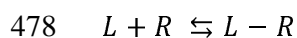
417 Explicit solvent MD simulation were run using NAMD 2.12 (24) software, applying the
418 Amber force field (ff14SB) (25). The TIP3P (26) water solvent model was used. The
419 t-leap application of the Ambertools 14.0 package (25) was applied to generate the
420 topology, the parameters, and the coordinate files of the macromolecular complex
421 simulated. The coordinates of the macromolecular elements of the nsp12/7/8
422 complex: nsp12, nsp8, nsp7, pyr, template RNA, nascent strand RNA, were
423 extracted from the PDB 7bv2. The geometries of the VR17-04, enisamium (before
424 docking) and pyr were optimized using the quantum chemical approach DFT
425 B3LYP/6-31G*; the corresponding partial charges were estimated fitting the
426 electrostatic potential that was calculated at level of theory B3LYP/6-31G*/RHF/6-
427 31G*. This procedure is in accord to the standard required by the Amber force field.
428 The quantum chemistry software GAMESS (27) was used for this stage. The Amber
429 atomtypes (parm10.dat) were selected for VR17-04, enisamium and pyr
430 (antechamber application, Ambertools 14.0). Three macromolecular complexes
431 indicated as VR1704-nsp12/7/8(Cyt), enisamium-nsp12/7/8(Cyt), and VR1704-
432 nsp12/7/8(Ade), were solvated by a 15 Å wide layer of TIP3P water molecules in
433 each X, Y, Z direction; the orthogonal simulation box was built with hedges of
434 approximate length 116, 116, 127 Å. The non-bond electrostatic and dispersive
435 interactions were described by the standard cut-off technique (12.0 Å). Before
436 running MD simulation, each simulation cell box was energy minimized running 200
437 K steps of the default energy minimized algorithm, as implemented in NAMD. The
438 MD simulations were run fixing the number of particle (N), the absolute temperature
439 (T), and the pressure (P) applied to the cell hedges. The absolute temperature was
440 300 K and maintained with a Lowe–Andersen thermostat, while the pressure on the
441 cell box hedges was set as $P = 1.01325$ bar and preserved by the Nosé–Hoover–

442 Langevin piston algorithm. The first MD simulation stage was run to adjust the
443 simulation cell box density, allowing the relaxation of all the inter-molecule distances,
444 i.e., the solute-solute, solute-solvent, and solvent-solvent distances. The cell density
445 equilibration stage was run restraining the atoms of the solute to their initial position
446 (energy minimized geometry of the complex) applying a harmonic restraint. In this
447 stage of cell density equilibration, the water molecules were left free to move. The
448 harmonic restraint constant value was set initially as 1 Kcal mol⁻¹ for each atom of
449 the solute, and progressively reduced at 0.5 and 0.2 Kcal mol⁻¹. The cell density
450 equilibration stage was monitored plotting the cell volume (Å³) vs time (ns), until the
451 cell volume fluctuations level-off to a horizontal axis that corresponds to the average
452 final volume of the cell. This stage required between 20 to 50 ns approximately and
453 was further checked by the formation of a thin water shell that surround the face of
454 the inhibitor molecule that is exposed to the empty catalytic cavity of the nsp12/7/8
455 complex. In the second stage of the MD simulation, the harmonic restraint was
456 removed, and the inhibitor-nsp12/7/8 complex was allowed to equilibrate in the
457 geometry and the relative position of their elements: inhibitor, template RNA, nascent
458 strand RNA, pyr, Mg⁺², and Zn⁺². To monitor the equilibration of position and
459 orientation that VR17-04 (or enisamium) presents in the +1 position of the catalytic
460 cavity, the distances between the carbonyl oxygen of VR17-04 and the hydrogen
461 (NH₂-) of cytosine (or adenine), and between the hydroxyl group of VR17-04 and the
462 nearby lone pair of cytosine nitrogen (or adenine), were plotted vs simulation time.
463 These distances provide a direct indication of the stability of the Watson-Crick base
464 pair interaction that hold the inhibitor and the target base. The orientation of the
465 VR17-04 in the catalytic site of the nsp12 were also monitored by the improper
466 dihedral angle ϕ defined by the following atoms (bold) **CO-NH₂-N-OH**, in which **CO**
467 and **OH** belong to VR17-04, while the remaining **NH₂** and **N** belong to the opposite
468 cytosine (or adenine). Alternatively, the enisamium-cytosine pair require the following
469 atoms **CO-NH₂-N-CH** to define ϕ , in this case **CO** and **CH** belong to enisamium,
470 while **NH₂** and **N** belong to the opposite cytosine. In fact, values of this angle around
471 '0' indicate that the 'base pair' contact between VR1704 the cytosine (or adenine) is
472 coplanar, a geometric condition favouring the Watson-Crick 'base-pair' interaction
473 between VR17-04 and the base. VMD 1.9.3 (28) was used for the MD simulation
474 trajectory visualization and image creation.

475

476 **Estimation of Poisson-Boltzmann free energy of binding**

477 In a system that evolve in accord to the complex formation reaction (29).



479 **(eq. 1)**

480 The free energy change is calculated knowing only the initial and final state of the
481 system:

$$482 \quad \Delta G^{Bind} = G(L - R) - G(L) - G(R)$$

483 **(eq. 2)**

484 The free energy decomposed in the following terms:

$$485 \quad G = \langle E_{MM} \rangle + \langle G_{sol} \rangle + \langle G_{noPol} \rangle - T \langle S_{MM} \rangle \quad \text{(eq. 3)}$$

486 The free energy change is then conveniently split:

$$487 \quad \Delta G^{Bind} = \Delta G_{PB}^{Bind} + \Delta S_{MM} \quad \text{(eq. 4)}$$

488 In **eq. 3** the E_{MM} correspond to the potential energy of the system, as described by
489 the force-field; G_{sol} is the polar solvation energy, estimated by the Poisson-
490 Boltzmann equation (30); G_{noPol} is the non-polar solvation energy, estimated by the
491 solvent-accessible surface area, a method included in the MMPBSA. T is the
492 absolute equilibrium temperature, while S_{MM} is the molecular entropy of the system.
493 The sum of the first three terms on the right-hand side of the **eq. 3** is conveniently
494 defined Poisson-Boltzmann free energy of binding ΔG_{PB}^{Bind} (see **eq. 4**). To estimate
495 the absolute value of the free energy of binding ΔG^{Bind} the molecular entropy change
496 ΔS_{MM} is required. Since in this study two similar molecules: VR17-04 and enisamium
497 were compared as bound to cytosine (+1 position of the catalytic site of nsp12), or
498 alternatively two bound states VR17-04-cytosine or VR17-04-adenine were inquired,
499 in a level zero approximation the respective entropy changes ΔS_{MM} are considered
500 similar. In this condition the Poisson-Boltzmann free energy of binding ΔG_{PB}^{Bind} could
501 be used to rank the selected molecular recognitions and/or the poses of the docking
502 experiment.

503

504 **Patients**

505 For this prospective, multi-centre, randomized, double-blind, placebo-controlled,
506 parallel-group phase III clinical trial, male and female hospitalized patients ≥ 18
507 years with moderate severity of COVID-19 infection were eligible for participation.

508 The diagnosis of COVID-19 was based on body temperatures of ≥ 37.8 °C and
509 laboratory confirmed RT-PCR SARS-CoV-2 test from pharyngeal swabs or sputum.
510 According to intent-to-treat (ITT) definition and the actual recruitment status, 373
511 patients from 15 Ukrainian hospitals could be included into the interim analysis.

512 The study was conducted in accordance with the Declaration of Helsinki, ICH-
513 GCP and the national laws and regulations in Ukraine. All patients signed an
514 informed consent prior to study participation. The study was approved by the Ethics
515 Commission of the Regional Clinical Hospital of Ivano-Frankivsk Regional Council on
516 12.05.2020. The registration number of the study in ClinicalTrials.gov is
517 NCT04682873.

518

519 ***Treatment***

520 Patients were randomized at a 1:1 ratio to receive either 500 mg enisamium chloride
521 or matching placebo 4 times daily every 6 h for 7 full days. Supporting treatment
522 could be given at the investigator's discretion. All patients treated with either placebo
523 or enisamium, having a laboratory-confirmed SARS-CoV-2 at randomization and
524 providing any valid efficacy data after initiation of treatment were included in the
525 Intent-to-Treat evaluation set (ITT).

526

527 ***Data Collection***

528 Baseline clinical data of the patients were recorded in the electronic case report
529 forms including demographics, medical history, previous and ongoing medication,
530 body height and weight and results of physical examination. During the study up to
531 day 29 or until discharge, symptom severity rating, vital signs, assessment of
532 COVID-19 symptoms, safety lab results, concomitant medication and adverse events
533 were recorded. The patient's and investigator's judgment on safety and efficacy were
534 collected independently. RT-PCR tests on SARS-CoV-2 at defined intervals and at
535 the discretion of the investigator were carried out.

536

537 ***Primary Outcome***

538 The primary outcome was measured as the time from the day of randomization (day
539 1) to an improvement of at least two score points (from the status at randomization)
540 on the severity rating (SR) scale in days. The SR scale (WHO scale) is defined as 1
541 (8) - Death; 2 (7, 6) - Hospitalized, on invasive mechanical ventilation or

542 extracorporeal membrane oxygenation; 3 (5) - Hospitalized, on non-invasive
543 ventilation or high flow oxygen; 4 (5) - Hospitalized, requiring supplemental oxygen;
544 5 (3) - Hospitalized, not requiring supplemental oxygen – requiring ongoing medical
545 care; 6 (-) - Hospitalized, not requiring supplemental oxygen – no longer requires
546 ongoing medical care; 7 (2) - Not hospitalized, limitation on activities and/or requiring
547 home oxygen; 8 (1) - Not hospitalized, no limitations on activities. Safety of
548 enisamium iodide will be analysed based on the incidence of adverse events, vital
549 signs, judgement of global tolerability on day of hospital discharge (separately by
550 patient and investigator) and laboratory data when the study is completed.

551

552 ***Statistical Analysis of Interim Data.***

553 The unblinded interim analysis was carried out by an Independent Data Monitoring
554 Committee based on a pre-specified Charter. At this stage, the primary outcome was
555 pre-planned to be tested by using the two-sided log-rank test stratified by centre.
556 Because of the low patient number in some centres the stratification was omitted for
557 gaining primary interim results. The primary outcome was defined as an
558 improvement from baseline of at least two SR points and was evaluated for all ITT
559 patients at the interim stage as well as for subgroups with baseline score of SR 4
560 and 5 separately. The interim analysis used the promising zone approach according
561 to (31) that was implemented according to (32). For this method no adjustment of the
562 type-I error rate is needed.

563

564 **Acknowledgments**

565 The authors would like to thank Dr. Juergen Richt (Kansas State University,
566 Manhattan, KS, US) for comments and advice, and Dr Ervin Fodor, Dr Jonathan
567 Grimes, Alexander Walker, Dr Haitian Fan and Dr Jeremy Keown (University of
568 Oxford, Oxford, UK) for expression constructs and sharing preliminary data.

569

570 **Funding**

571 A.J.W.t.V is supported by joint Wellcome Trust and Royal Society grant
572 206579/Z/17/Z and the National Institutes of Health grant R21AI147172. Part of this
573 research was funded by Farmak Public Joint Stock Company, Kiev, Ukraine.

574

575 **Conflict of interest**

576 V.M. and A.G. are employees of Farmak Public Joint Stock Company, Kiev, Ukraine.
577 Part of this research was funded by Farmak Public Joint Stock Company, Kiev,
578 Ukraine.

579
580

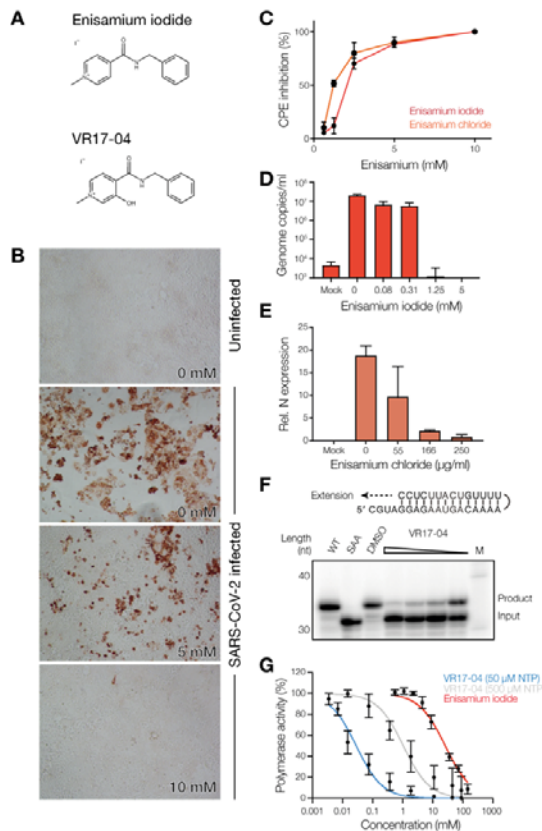
581 References

- 582 1. T. P. Sheahan *et al.*, An orally bioavailable broad-spectrum antiviral inhibits SARS-CoV-2 in
583 human airway epithelial cell cultures and multiple coronaviruses in mice. *Sci Transl Med*
584 10.1126/scitranslmed.abb5883 (2020).
- 585 2. R. M. Cox, J. D. Wolf, R. K. Plemper, Therapeutically administered ribonucleoside analogue
586 MK-4482/EIDD-2801 blocks SARS-CoV-2 transmission in ferrets. *Nat Microbiol*
587 10.1038/s41564-020-00835-2 (2020).
- 588 3. A. Shannon *et al.*, Rapid incorporation of Favipiravir by the fast and permissive viral RNA
589 polymerase complex results in SARS-CoV-2 lethal mutagenesis. *Nat Commun* **11**, 4682
590 (2020).
- 591 4. D. H. Goldhill *et al.*, The mechanism of resistance to favipiravir in influenza. *Proc Natl Acad*
592 *Sci U S A* **115**, 11613-11618 (2018).
- 593 5. E. Hartenian *et al.*, The molecular virology of coronaviruses. *J Biol Chem* **295**, 12910-12934
594 (2020).
- 595 6. V. Coronaviridae Study Group of the International Committee on Taxonomy of, The species
596 Severe acute respiratory syndrome-related coronavirus: classifying 2019-nCoV and naming it
597 SARS-CoV-2. *Nat Microbiol* **5**, 536-544 (2020).
- 598 7. L. Subissi *et al.*, SARS-CoV ORF1b-encoded nonstructural proteins 12-16: replicative enzymes
599 as antiviral targets. *Antiviral Res* **101**, 122-130 (2014).
- 600 8. A. J. te Velhuis, J. J. Arnold, C. E. Cameron, S. H. van den Worm, E. J. Snijder, The RNA
601 polymerase activity of SARS-coronavirus nsp12 is primer dependent. *Nucleic Acids Res* **38**,
602 203-214 (2010).
- 603 9. L. Subissi *et al.*, One severe acute respiratory syndrome coronavirus protein complex
604 integrates processive RNA polymerase and exonuclease activities. *Proc Natl Acad Sci U S A*
605 **111**, E3900-3909 (2014).
- 606 10. L. Yan *et al.*, Architecture of a SARS-CoV-2 mini replication and transcription complex. *Nat*
607 *Commun* **11**, 5874 (2020).
- 608 11. H. S. Hillen *et al.*, Structure of replicating SARS-CoV-2 polymerase. *Nature* **584**, 154-156
609 (2020).
- 610 12. J. Chen *et al.*, Structural Basis for Helicase-Polymerase Coupling in the SARS-CoV-2
611 Replication-Transcription Complex. *Cell* **182**, 1560-1573 e1513 (2020).
- 612 13. T. G. Zubkova *et al.*, Enisamium reduces influenza virus shedding and improves patient
613 recovery by inhibiting viral RNA polymerase activity. *MedRxiv* (2020).
- 614 14. A. P. Walker *et al.*, Enisamium is a small molecule inhibitor of the influenza A virus and SARS-
615 CoV-2 RNA polymerases. *bioRxiv* 10.1101/2020.04.21.053017 (2020).
- 616 15. D. Boltz *et al.*, Activity of enisamium, an isonicotinic acid derivative, against influenza viruses
617 in differentiated normal human bronchial epithelial cells. *Antivir Chem Chemother* **26**,
618 2040206618811416 (2018).
- 619 16. J. H. Beigel *et al.*, Remdesivir for the Treatment of Covid-19 - Final Report. *N Engl J Med* **383**,
620 1813-1826 (2020).
- 621 17. V. V. Zurbaev, A. V. Slita, E. O. Sinegubova, A. A. Muryleva, I. N. Lavrentieva, Anti-viral
622 activity of enisamium iodide against viruses of influenza and ARVI's on different cell lines.
623 *Therapeutic Archive* **92**, 45-50 (2020).
- 624 18. D. Bojkova *et al.*, Proteomics of SARS-CoV-2-infected host cells reveals therapy targets.
625 *Nature* **583**, 469-472 (2020).
- 626 19. D. Bojkova *et al.*, Aprotinin Inhibits SARS-CoV-2 Replication. *Cells* **9** (2020).

- 627 20. T. Toptan *et al.*, Optimized qRT-PCR Approach for the Detection of Intra- and Extra-Cellular
628 SARS-CoV-2 RNAs. *Int J Mol Sci* **21** (2020).
- 629 21. G. M. Morris *et al.*, AutoDock4 and AutoDockTools4: Automated docking with selective
630 receptor flexibility. *J Comput Chem* **30**, 2785-2791 (2009).
- 631 22. W. Yin *et al.*, Structural basis for inhibition of the RNA-dependent RNA polymerase from
632 SARS-CoV-2 by remdesivir. *Science* **368**, 1499-1504 (2020).
- 633 23. J. Gesteiger, M. Marsili, Iterative partial equalization of orbital electronegativity a rapid
634 access to atomic charges. *Tetrahedron* **36**, 3219-3228 (1980).
- 635 24. J. C. Phillips *et al.*, Scalable molecular dynamics with NAMD. *J Comput Chem* **26**, 1781-1802
636 (2005).
- 637 25. D. A. Case *et al.*, The Amber biomolecular simulation programs. *J Comput Chem* **26**, 1668-
638 1688 (2005).
- 639 26. W. L. Jorgensen, J. Chandrasekhar, J. D. Madura, R. W. Impey, M. L. Klein, Comparison of
640 simple potential functions for simulating liquid water *J. Chem. Phys.* **79**, 926-935 (1983).
- 641 27. M. W. Schmidt *et al.*, General Atomic and Molecular Electronic Structure System. *J. Comput.*
642 *Chem.* **14**, 1347-1363 (1993).
- 643 28. W. Humphrey, A. Dalke, K. Schulten, VMD: visual molecular dynamics. *J. Mol. Graphics* **14**,
644 27-38 (1996).
- 645 29. A. Weis, K. Katebzadeh, P. Söderhjelm, I. Nilsson, U. Ryde, Ligand affinities predicted with
646 the MM/PBSA method: dependence on the simulation method and the force field. *J. Med.*
647 *Chem.* **49**, 6596-6606 (2006).
- 648 30. J. Srinivasan, T. E. Cheatham, III, T. E. Cieplak, P. Kollman, D. A. Case, Continuum solvent
649 studies of the stability of DNA, RNA, and phosphoramidate–DNA helices. *J. Am. Chem. Soc.*
650 **120**, 9401-9409 (1998).
- 651 31. C. R. Mehta, S. J. Pocock, Adaptive increase in sample size when interim results are
652 promising: a practical guide with examples. *Stat Med* **30**, 3267-3284 (2011).
- 653 32. P. Broberg, Sample size re-assessment leading to a raised sample size does not inflate type I
654 error rate under mild conditions. *BMC Med Res Methodol* **13**, 94 (2013).
- 655
656

657 **Figures and legends**

658



659

660

Figure 1. Enisamium inhibits SARS-CoV-2 infection and replication *in vitro*.

661

Chemical structures of FAV00A and VR17-04. The chemical structure of FAV00B is

662

identical to FAV00A except that chloride ions are present instead of iodide. **(B)**

663

Inhibition of SARS-CoV-2 N expression in Caco-2 cells by enisamium chloride. **(C)**

664

Inhibition of SARS-CoV-2 cytopathic effect in Caco-2 cells by enisamium iodide and

665

chloride. **(D)** Quantification of SARS-CoV-2 RNA genome levels in NHBE cells

666

infected with SARS-CoV-2 after treatment with enisamium iodide. **(E)** Quantification

667

of HCoV-NL63 N mRNA levels in NHBE cells infected with HCoV-NL63 after

668

treatment with enisamium chloride. **(F)** Inhibition of the SARS-CoV-2 nsp12/7/8 RNA

669

polymerase complex by VR17-04 on a hairpin template. A mutant containing a

670

double amino acid substitution in the nsp12 active site (SDD=>SAA) was used as

671

negative control. DMSO was used as solvent control. **(G)** Quantification of SARS-

672

CoV-2 nsp12/7/8 RNA polymerase complex inhibition by enisamium or VR17-04 on

673

a hairpin template. For VR17-04 two nucleotide triphosphate concentrations were

674

used. Polymerase activity was plotted against drug concentration and dose-response

675

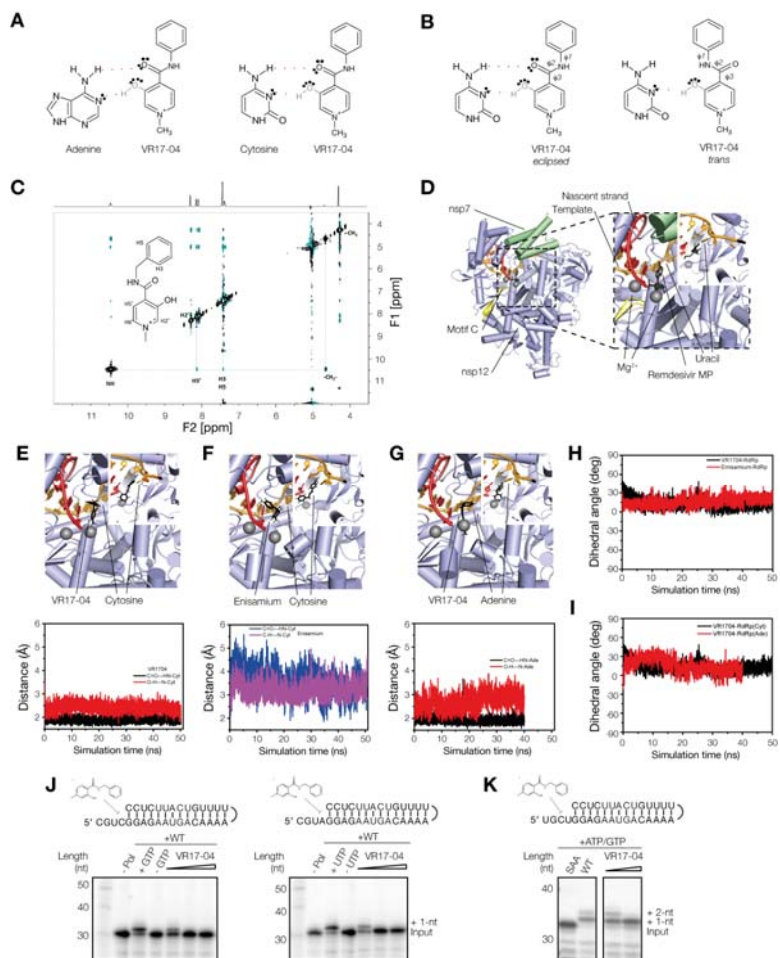
curves were fit to the data. Quantification is from n=3 independently prepared

676

reactions using the same nsp12/7/8 protein preparation. Error bars represent

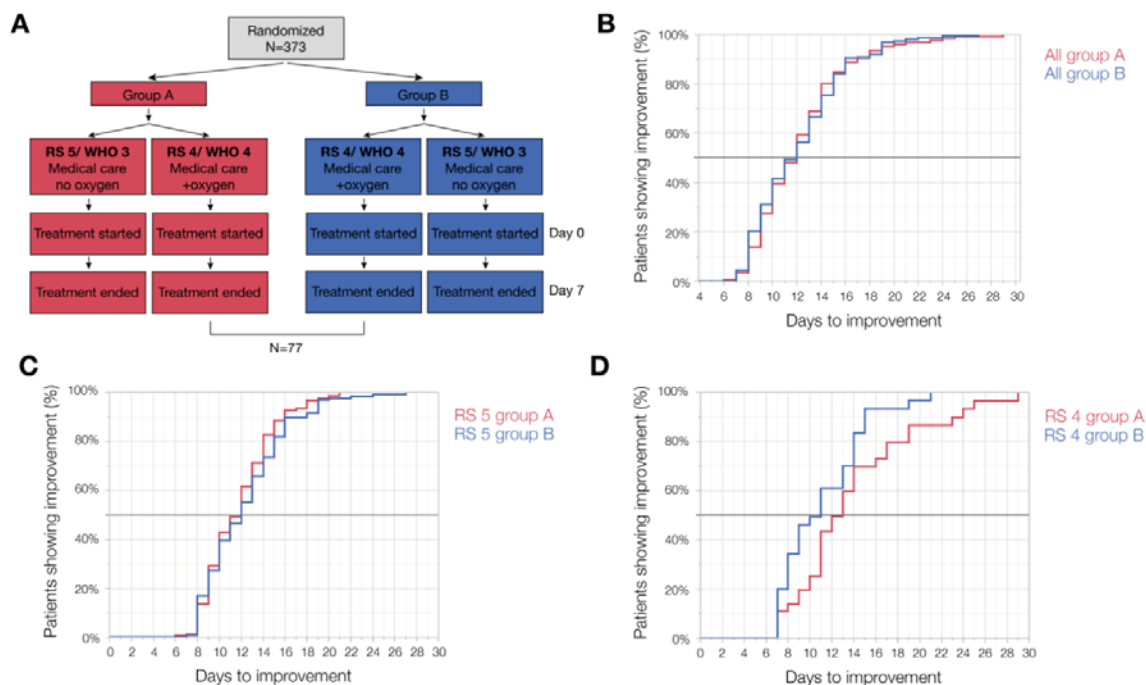
677

standard deviation.



678
679
680
681
682
683
684
685
686
687
688
689
690
691
692
693
694
695
696
697

Figure 2. Enisamium metabolite VR17-04. (A) Schematic of putative hydrogen bond formation between cytosine and adenine bases with VR17-04. (B) Schematic of the *trans* and *eclipsed* conformations of VR17-04. (C) 2D-NOESY and 1H proton (above) spectra of VR17-04 acquired at 277 K in water. The NOE correlation between the HN and H5' proton is highlighted with a dashed line. (D) Structure of the SARS-CoV-2 nsp12/7/8 complex bound to RNA and remdesivir monophosphate. Rendering based on PDB 7bv2. (E) Model (top) and MD simulation (bottom) of VR17-04 binding to cytosine in nsp12 active site. (F) Model (top) and MD simulation (bottom) of enisamium binding to cytosine in nsp12 active site. (G) Model (top) and MD simulation (bottom) of VR17-04 binding to adenine in nsp12 active site. (H) MD simulation of dihedral angle of VR17-04 or enisamium binding to cytosine in nsp12 active site. (I) MD simulation of dihedral angle of VR17-04 binding to cytosine or adenine in nsp12 active site (J) Effect of VR17-04 on SARS-CoV-2 nsp12/7/8 activity on two different hairpin templates in the presence of GTP (left) or UTP (right). In the presence of wildtype nsp12/7/8 and GTP or UTP, the radiolabelled primer was extended by 1 nt. (K) Effect of VR17-04 on SARS-CoV-2 nsp12/7/8 primer extension activity. A mutant containing a double amino acid substitution in the nsp12 active site (SDD=>SAA) was used as negative control. ATP and GTP were added to the reaction to allow extension of the template by 2 nt.



698

699

700

701

702

703

704

Figure 3. Enisamium improves recovery of COVID-19 patients requiring supplementary oxygen. (A) Schematic of patient recruitment, randomization and treatment. (B) Kaplan-Meier plot of the percentage improvement observed in all COVID-19 patients, (C) RS 5 COVID-19 patients (medical care with no oxygen support), and (D) RS 4 COVID-19 patients (medical care with non-invasive oxygen support).